Progress In Electromagnetics Research, Vol. 175, 13–27, 2022

An Elliptically Polarized Wave Injection Technique via TF/SF Boundary in Subdomain Level DGTD Method

Xiaobing Han[1], Hang Li[1], Yuanguo Zhou[1, *], Lin Wang[2], Shangqing Liang[2], and Fawad Javaid[3]

Abstract—This study presents an effective solution on the basis of Discontinuous-Galerkin Time-Domain (DGTD) scheme for the injection of elliptically polarized plane wave through total-field/scattered-field (TF/SF) boundary. Generally, the elliptically polarized wave can be resolved into two linearly polarized waves in phase quadrature with the polarization planes at right angles to each other, but the proposed methodology is focused to utilize the principle of wave field formation to induce left-handed or right-handed elliptically polarized waves by regulating the phase and amplitude of the incident waves. The outcome of the proposed technique is achieved by deriving the EB-scheme equations and employing the explicit fourth order Runge-Kutta (RK4) time integration scheme in the DGTD methodology. An anisotropic Riemann solver and non-conformal mesh schemes are introduced for domain decomposition to allow efficient spatial discretization. Additionally, the proposed work is extended from single frequency to broadband elliptical polarized plane wave injection in the DGTD method, and the significance of this study is observed in the results. The experimental outcomes reveal that the proposed method is consistent with the analytical solution in free space and expected to provide efficient numerical solutions for analyzing scattering characteristics generated by various elliptically polarized waves.

1. INTRODUCTION

The polarization of electromagnetic wave refers the nature of its orientation and the change in amplitude of electromagnetic field intensity with time. In information detection systems such as remote sensing and radar target recognition, the polarization of scattered wave can also provide additional information besides amplitude and phase information. Common engineering applications such as weather radar, altitude radar, and interception radar of detection flight vehicle usually use horizontal polar wave whereas sea navigation radar and ground/sea search radar on aircraft mostly use vertical polarized wave. In recent years, it has been observed that circular polarization wave can suppress the interference of rain and fog, resist multi-path reflection, and have the advantages of better mobility. It has been widely used in various application including satellite communication, radar technologies, mobile communication, and various other wireless communication protocols. However, the research on the technique of generating broadband circularly polarized plane waves is relatively less focused in numerical simulations. In electromagnetic simulation, the total-field/scattered-field (TF/SF) technique is the most conventional and available approach to mitigate the challenge of scattering by introducing linearly polarized plane waves [1, 2]. According to the discontinuity technique and the equivalence principle of the Maxwell's equations, the calculated region can be classified into the total field region and scattering field region. The total field is composed of both incident field and scattering field while the scattering field only

Received 22 February 2022, Accepted 16 June 2022, Scheduled 21 July 2022

* Corresponding author: Yuanguo Zhou (wingkoo@foxmail.com).

[1] College of Communication and Information Engineering, Xi'an University of Science and Technology, Xi'an 710054, China. [2] College of Electronics and Information, Hangzhou Dianzi University, China. [3] Department of Computing and Information Technology, University of Gujrat, Pakistan.

retains scattering field. Therefore, this method is very feasible if only the scattering characteristics of the target are desired such as calculating the radar scattering cross section (RCS) of the target. By using the equivalence principle, the incident field of the total fields is susceptible to the interface between the total field and scattering field that is generally called the Huygens' plane or the tangential field on the connecting boundary. Thus, a three-dimensional (3-D) volume source problem can be transformed into a two-dimensional (2-D) surface source problem.

To efficiently implement the TF/SF technique in the finite difference time domain (FDTD) method, 1D incident field array (IFA) method is proposed in [2]. In this method, plane waves are first simulated on a one-dimensional grid, and then the incident field of the field points around the connecting boundary is gradually obtained by interpolation and projection over time to introduce plane waves into the total field region. A study in [3] provides a framework for a perfect TF/SF boundary for pulsed plane waves that do not propagate in a grid-aligned fashion, and it claimed to be more accurate than previously proposed 1-D auxiliary schemes. Similarly, a research was presented in [4] that introduced a new staggered field design and formulation for the 1-D propagator of the TF/SF source implementation in FDTD scattering simulation. A research in [5] presented the optimized analytic field propagator (O-AFP) method for plane wave injection in the FDTD simulations. The proposed approach has addressed the accuracy and memory storage issues faced by the existing TF/SF formulation. In [6], an FDTD discrete plane wave (FDTD-DPW) technique is proposed for the generation of plane waves in the TF/SF formulation of the FDTD method. Correspondingly, a study in [7] proposed a new generalized total-field/scattered-field (G-TF/SF) formulation to model an infinite material scattering illuminated by an arbitrarily oriented plane wave within a compact FDTD grid. In [8], a plane-wave injector (TF/SF boundary) for a general layered medium was presented. The proposed work in [9] described a new finite-element time-domain (FETD) volumetric plane-wave excitation method for use with the total-and-scattered-field decomposition (TSFD). This method provides an alternative to the traditional Huygens' surface approaches commonly used to impress the incident field into the total-field region.

On the other hand, the Discontinuous-Galerkin Time-Domain (DGTD) method [10–25] to estimate the mutual characteristics of the finite volume time domain (FVTD) method [26] and the FETD method [27, 28] have many advantages in dealing with complex and fine structure with high accuracy. As an extension of the isotropic DGTD methods [29, 30], the recently emerging anisotropic subdomain level DGTD method exhibits more advantages [31, 32] including non-conformal mesh that can alleviate meshing difficulties for large scale problems, and **EB**-scheme that is more efficient than the **EH**-scheme. In the subdomain level of DGTD method, the different-structured elements can be used to classify the calculation of domain into non-overlapping elements and the adjacent elements. It can be discretized by employing non-conformal meshes or interpolating by basic functions of different orders to attain high efficiency and accuracy. The anisotropic numerical flux is introduced to exchange energy instead of satisfying the condition of tangential continuity between one element and its adjacent elements. The algorithm is quasi explicit in space and only needs to inverse multiple matrices whose dimensions are the numbers of basic functions in the elements.

In this work, we presents an analytic solution for the injection of elliptically polarized plane wave via TF/SF boundary and employs the electric field intensity **E** and magnetic flux density **B** to solve the Maxwell's equations. To achieve this objective, the proposed method utilizes the principle of wave field formation to generate left-handed or right-handed elliptically polarized waves by regulating the phase and amplitude of the incident waves. Particularly, the study is focused to derive the **EB**-scheme based analytic solutions of plane waves, and explicit fourth order Runge-Kutta (RK4) time integration scheme is utilized in the subdomain level of DGTD method. The anisotropic Riemann solver and non-conformal mesh are introduced for domain decomposition to allow efficient spatial discretization. Furthermore, we extend this method from single frequency to broadband elliptically polarized plane wave injection in the DGTD method.

2. METHODOLOGY

2.1. EB-Scheme Based Analytic Solutions of Plane Waves

To introduce the plane wave into DGTD algorithm via TF/SF boundary, we derive the solution of the plane wave in the inhomogeneous medium in this section. The **EB**-scheme Maxwell's equations can be

expressed as

$$\nabla \times \bar{\bar{\mu}}^{-1} \cdot \nabla \times \mathbf{E} - \omega^2 \bar{\bar{\varepsilon}} \cdot \mathbf{E} = 0 \tag{1}$$

$$\nabla \times \bar{\bar{\varepsilon}}^{-1} \cdot \nabla \times \left(\bar{\bar{\mu}}^{-1}\mathbf{B}\right) - \omega^2 \mathbf{B} = 0 \tag{2}$$

where $\mathbf{E}$ and $\mathbf{B}$ represent the electric field intensity and magnetic flux density, respectively. $\bar{\bar{\varepsilon}}$ and $\bar{\bar{\mu}}$ are permittivity and permeability of the medium, respectively, and ω denotes the angular frequency. Assuming that $\mathbf{k}$ is the vector wave number in the propagation direction of the plane wave, the expression of electric field and magnetic flux density can be written as

$$\mathbf{E} = \mathbf{E}_0 e^{i\mathbf{k}\cdot\mathbf{r}} \tag{3}$$

$$\mathbf{B} = \mathbf{B}_0 e^{i\mathbf{k}\cdot\mathbf{r}} \tag{4}$$

Substitute (3) and (4) into (1) and (2), respectively, to obtain

$$\mathbf{k} \times \bar{\bar{\mu}}^{-1} \cdot \mathbf{k} \times \mathbf{E}_0 + \omega^2 \bar{\bar{\varepsilon}} \cdot \mathbf{E}_0 = 0 \tag{5}$$

$$\mathbf{k} \times \bar{\bar{\varepsilon}}^{-1} \cdot \mathbf{k} \times \bar{\bar{\mu}}^{-1}\mathbf{B}_0 + \omega^2 \cdot \mathbf{B}_0 = 0 \tag{6}$$

Let's take $\mathbf{E}$ as an example, and $\mathbf{k} \times \mathbf{E}$ can be expressed as $\widetilde{\mathbf{K}} \cdot \mathbf{E}_0$, where

$$\widetilde{\mathbf{K}} = \begin{bmatrix} 0 & -k_z & k_y \\ k_z & 0 & -k_x \\ -k_y & k_x & 0 \end{bmatrix} \tag{7}$$

Each Cartesian component of the above formula can be represented by a directional cosine, thus

$$\widetilde{\mathbf{K}}(\theta,\varphi) = |k| \cdot \begin{bmatrix} 0 & -\cos\theta & \sin\theta\sin\varphi \\ \cos\theta & 0 & -\sin\theta\cos\varphi \\ -\sin\theta\sin\varphi & \sin\theta\cos\varphi & 0 \end{bmatrix} \tag{8}$$

where $|k|$ is the magnitude of vector $\mathbf{k}$. On the top of that, (5) can be written as

$$\left[|k|^2 \cdot \widetilde{\mathbf{F}}(\theta,\varphi) + \omega^2 \cdot \bar{\bar{\mathbf{I}}}\right] \cdot \mathbf{D}_0 = 0 \tag{9}$$

where

$$\widetilde{\mathbf{F}}(\theta,\varphi) = |k|^{-2}\, \widetilde{\mathbf{K}}(\theta,\varphi) \cdot \bar{\bar{\mu}}^{-1} \cdot \widetilde{\mathbf{K}}(\theta,\varphi) \cdot \bar{\bar{\varepsilon}}^{-1}, \mathbf{D}_0 = \bar{\bar{\varepsilon}} \cdot \mathbf{E}_0 \tag{10}$$

where $\bar{\bar{\mathbf{I}}}$ denotes the unitary matrix, and $\widetilde{\mathbf{F}}(\theta,\varphi)$ is a function of angles and electrical tensors of the medium. Thus, for a plane wave propagating in a certain direction, $\widetilde{\mathbf{F}}(\theta,\varphi)$ is just a constant matrix.

As we can see, Equation (9) corresponds to an eigenvalue problem, where ω^2/k^2 is the eigenvalue, and $\mathbf{D}_0$ is the eigenvector. Based on the condition $\nabla \cdot \mathbf{D} = 0$, we have $\mathbf{k} \cdot \mathbf{D} = 0$, thus, only two of the three components of the electric flux density $\mathbf{D}$ are independent. This means that Equation (9) contains two independent equations; therefore, (9) only has two eigenvalues and eigenvectors. Then, the general solution of Equation (1) can be expressed as

$$\mathbf{E} = a_1\mathbf{e}_1 e^{i\mathbf{k}_1\cdot\mathbf{r}} + a_2\mathbf{e}_2 e^{i\mathbf{k}_2\cdot\mathbf{r}} = \sum_{i=1}^{n} a_j\mathbf{e}_j e^{i\mathbf{k}_j\cdot\mathbf{r}} \tag{11}$$

where a_1 and a_2 are the magnitudes of the electric field; $\mathbf{e}_1$ and $\mathbf{e}_2$ are two linearly independent vectors. Since vectors $\mathbf{e}_1$, $\mathbf{e}_2$, and $\mathbf{k}$ are orthogonal to each other, (11) can be written as

$$\mathbf{E} = a_1(\mathbf{k} \times \boldsymbol{\eta})e^{i\mathbf{k}\cdot\mathbf{r}} + a_2(\mathbf{k} \times \mathbf{k} \times \boldsymbol{\eta})e^{i\mathbf{k}\cdot\mathbf{r}} \tag{12}$$

where $\boldsymbol{\eta}$ is an arbitrary direction vector. If $\boldsymbol{\eta}$ points in the z-direction, for example, the two wave components in (12) correspond to the transverse electric (TE) wave and transverse magnetic (TM) wave, respectively.

As the magnetic flux density is orthogonal to the electric field, we have

$$\mathbf{B} = b_1(\mathbf{k} \times \mathbf{k} \times \boldsymbol{\eta})e^{i\mathbf{k}\cdot\mathbf{r}} + b_2(\mathbf{k} \times \boldsymbol{\eta})e^{i\mathbf{k}\cdot\mathbf{r}} \tag{13}$$

where b_1 and b_2 are the magnitudes of the magnetic flux density. By controlling the magnitudes, one can separately realize plane waves in TE or TM mode. In addition, by controlling the phase difference of the two orthogonal linearly polarized waves, one can implement circularly polarized plane waves. On this principle, this research realizes the injection of elliptically polarized plane wave into DGTD method by introducing the analytic solution of plane wave into the TF/SF boundary, as will be discussed later.

2.2. Subdomain Level Based Non-Conformal DGTD

The first order Maxwell's equations, involving electric field intensity $\mathbf{E}$ and magnetic flux density $\mathbf{B}$, can be expressed as

$$\varepsilon\frac{\partial \mathbf{E}}{\partial t}+\sigma_e\mathbf{E}+\mathbf{J}_s = \nabla\times\mu^{-1}\mathbf{B} \tag{14}$$

$$\frac{\partial \mathbf{B}}{\partial t}+\sigma_m\mu^{-1}\mathbf{B}+\mathbf{M}_s = -\nabla\times\mathbf{E} \tag{15}$$

$$\nabla\cdot\varepsilon\mathbf{E} = \rho_e \tag{16}$$

$$\nabla\cdot\mathbf{B} = \rho_m \tag{17}$$

where $\mathbf{J}_s$ and $\mathbf{M}_s$ are the electric and magnetic current densities due to imposed sources, while σ_e and σ_m are the material's electric conductivity and magnetic conductivity, respectively.

The DG method is applied to domain decomposition in the proposed **EB**-scheme DGTD method. After testing, the weak form of Maxwell's equations for the local subdomain is

$$\int_V \mathbf{\Phi}_i\cdot\left(\varepsilon\frac{\partial \mathbf{E}_i}{\partial t}+\sigma_e\mathbf{E}+\mathbf{J}_s^i\right)dV = \int_V \nabla\times\mathbf{\Phi}_i\cdot\mu^{-1}\mathbf{B}_i dV+\int_S \mathbf{\Phi}_i\cdot(\hat{\mathbf{n}}_i\times\mu^{-1}\mathbf{B}_t)dS \tag{18}$$

$$\int_V \mathbf{\Psi}_i\cdot\left(\frac{\partial \mathbf{B}_i}{\partial t}+\sigma_m\mu^{-1}\mathbf{B}_i+\mathbf{M}_s^i\right)dV = -\int_V \nabla\times\mathbf{\Psi}_i\cdot\mathbf{E}_i dV-\int_S \mathbf{\Psi}_i\cdot(\hat{\mathbf{n}}_i\times\mathbf{E}_t)dS \tag{19}$$

where $\mathbf{\Phi}$ and $\mathbf{\Psi}$ are the testing functions; $(\cdot)_i$ and $(\cdot)_t$ are the vectors for the ith subdomain field and total field, respectively; and $\hat{\mathbf{n}}_i$ is the unit outward vector on the boundary. When the integration region is in the volume, we have $(\cdot)_t=(\cdot)_i$. However, when the integration region is on the shared surfaces, $(\cdot)_t$ is from the contribution of both the ith subdomain and the jth subdomain.

To obtain the values of $\hat{\mathbf{n}}_i\times\mathbf{E}_t$ and $\hat{\mathbf{n}}_i\times\mu^{-1}\mathbf{B}_t$ in the above equations, the Riemann Solver [33–38] is employed

$$\hat{\mathbf{n}}_i\times\mathbf{E}_t = \frac{\hat{\mathbf{n}}_i\times(Y_i\mathbf{E}_i+Y_j\mathbf{E}_j)}{Y_i+Y_j}-\frac{\hat{\mathbf{n}}_i\times\hat{\mathbf{n}}_i\times(\mu_r^j\mathbf{B}_i-\mu_r^i\mathbf{B}_j)}{\mu_r^i\mu_r^j(Y_i+Y_j)} \tag{20}$$

$$\hat{\mathbf{n}}_i\times\mu_r^{-1}\mathbf{B}_t = \frac{\hat{\mathbf{n}}_i\times(\mu_r^j Z_i\mathbf{B}_i+\mu_r^i Z_j\mathbf{B}_j)}{\mu_r^i\mu_r^j(Z_i+Z_j)}-\frac{\hat{\mathbf{n}}_i\times\hat{\mathbf{n}}_i\times(\mathbf{E}_i-\mathbf{E}_j)}{Z_i+Z_j} \tag{21}$$

where ε_r^i and μ_r^i are relative permittivity and permeability of the ith subdomain, respectively. $Z_i=\sqrt{\mu_r^i}/\sqrt{\varepsilon_r^i}$ and $Y_i=1/Z_i$ are the impedance and admittance, respectively. By assembling the basis functions, the discrete matrix equations of subdomains can be obtained, and the linear system can be solved by adopting the explicit RK4 time stepping scheme.

2.3. Elliptically Polarized Wave Injection via TF/SF Boundary

In this section, a non-conformal mesh based TF/SF technique is presented for the elliptically polarized plane wave incidence at the physical region adjacent to the multiaxial perfectly matched layer (MPML) truncation [39–41]. We use the scattered and total fields as the unknowns for the MPML and physical regions, respectively, and the TF/SF interface is just the same as the interface between the MPML and physical region. As shown in Fig. 1, every basis function has a control point, where its value is maximal. Assume $\boldsymbol{\tau}_{TE,i}=[e_{TE,i1},\cdots,e_{TE,im},b_{TE,i1},\cdots,b_{TE,in}]^T$ or $\boldsymbol{\tau}_{TM,i}=[e_{TE,i1},\cdots,e_{TM,im},b_{TM,i1},\cdots,b_{TM,in}]^T$ are the unknown vectors for a physical subdomian with TE or TM incident wave, respectively, while $\boldsymbol{\tau}_{TE,j}=[e_{TE,j1},\cdots,e_{TE,jk},b_{TE,j1},\cdots,b_{TE,jl}]^T$ or $\boldsymbol{\tau}_{TM,j}=[e_{TM,j1},\cdots,e_{TM,jk},b_{TM,j1},\cdots,b_{TM,jl}]^T$ are the unknown vectors in its adjacent MPML subdomain with TE or TM incident wave, respectively. e and b are the unknowns, and T stands for the transpose. In addition, since the MPML region together with its interface uses the scattered field, incident plane waves need to be added here to obtain the total field.

To achieve elliptically polarized waves, the incident wave is projected to the basis functions in the jth subdomain via two orthogonal vectors and forms so-called 'incident vector' including

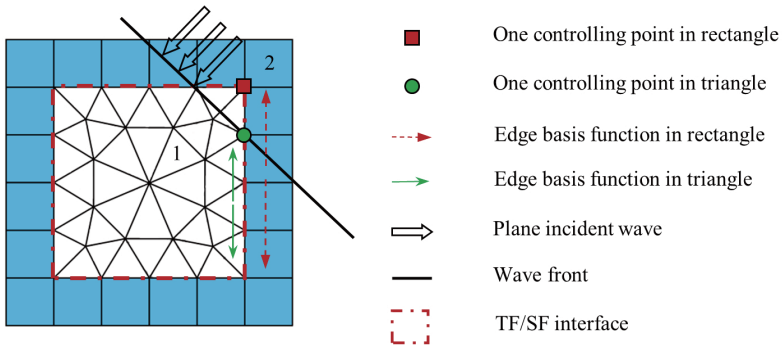

Figure 1. Total-field/scattered-field (TF/SF) technique for a non-conformal mesh. Group 1 representing the physical region is composed of triangles, and Group 2 representing the MPML region is composed of rectangles.

$\boldsymbol{\tau}_{TEinc,j} = [e_{TEinc,j1}, \cdots, e_{TEinc,jk}, b_{TE_{inc},j1}, \cdots, b_{TEinc,jl}]^T$ and $\boldsymbol{\tau}_{TMinc,j} = [e_{TMinc,j1}, \cdots, e_{TMinc,jk}, b_{TMinc,j1}, \cdots, b_{TMinc,jl}]^T$ where $e_{TEinc,p} = \langle \mathbf{E}_{TEinc}, \boldsymbol{\Phi}_{j,p} \rangle$, $e_{TMinc,p} = \langle \mathbf{E}_{TMinc}, \boldsymbol{\Phi}_{j,p} \rangle$, $b_{TEinc,p} = \langle \mathbf{B}_{TEinc}, \boldsymbol{\Psi}_{j,p} \rangle$ and $b_{TMinc,p} = \langle \mathbf{B}_{TMinc}, \boldsymbol{\Psi}_{j,p} \rangle$. $\mathbf{E}_{TEinc}$ and $\mathbf{B}_{TEinc}$ represent the electric field intensity and magnetic flux density in TE incident mode, respectively. $\mathbf{E}_{TMinc}$ and $\mathbf{B}_{TMinc}$ represent the electric field intensity and magnetic flux density in TM incident mode, respectively. $\boldsymbol{\Phi}$ and $\boldsymbol{\Psi}$ are the basis functions for $\mathbf{E}$ and $\mathbf{B}$, respectively.

Assuming that $f(t)$ is the time function of the plane wave, $l_{i,p}$ is the distance from the pth control point in the ith subdomain to the wave front at the time $t = 0$, and c is the wave speed in this medium. Thus, the time-varying illumination matrix can be defined as

$$\boldsymbol{\Lambda}_i = diag\left\{ f\left(t - \frac{l_{i,1}}{c}\right), \cdots, f\left(t - \frac{l_{i,m+n}}{c}\right) \right\} \tag{22}$$

Let's say $\boldsymbol{\eta}$ is pointing in the Cartesian z-axis, then $\mathbf{k} \times \boldsymbol{\eta}$ is corresponding to the horizontal polarization direction, while $\mathbf{k} \times \mathbf{k} \times \boldsymbol{\eta}$ is corresponding to the vertical polarization direction. As different illumination matrices need to be introduced in different polarization directions, (22) can be further decomposed into

$$\boldsymbol{\Lambda}_{\varphi_1,i} = diag\left\{ f_{\varphi_1}\left(t - \frac{l_{i,1}}{c}\right), \cdots, f_{\varphi_1}\left(t - \frac{l_{i,m+n}}{c}\right) \right\} \tag{23}$$

$$\boldsymbol{\Lambda}_{\varphi_2,i} = diag\left\{ f_{\varphi_2}\left(t - \frac{l_{i,1}}{c}\right), \cdots, f_{\varphi_2}\left(t - \frac{l_{i,m+n}}{c}\right) \right\} \tag{24}$$

where f_{φ_1} and f_{φ_2} represent plane wave functions with different initial phases. Then, the local subdomain system equations using TF/SF technique can be written as

$$\mathbf{M}_i \frac{d\boldsymbol{\tau}_{TE,i}}{dt} = \mathbf{L}_{ii}\boldsymbol{\tau}_{TE,i} + \sum_j \mathbf{L}_{ij}\boldsymbol{\tau}_{TE,j} + \boldsymbol{\Lambda}_{\varphi_1,i} \sum_j \mathbf{L}_{ij}\boldsymbol{\tau}_{TE_{inc},j} \tag{25}$$

$$\mathbf{M}_i \frac{d\boldsymbol{\tau}_{TM,i}}{dt} = \mathbf{L}_{ii}\boldsymbol{\tau}_{TM,i} + \sum_j \mathbf{L}_{ij}\boldsymbol{\tau}_{TM,j} + \boldsymbol{\Lambda}_{\varphi_2,i} \sum_j \mathbf{L}_{ij}\boldsymbol{\tau}_{TM_{inc},j} \tag{26}$$

where $\mathbf{M}_i$ is the mass matrices of the ith subdomain, and $\mathbf{L}_{ij}$ is composed of damping matrices. As different illumination matrices are introduced for the two incident vectors, the local subdomain system equations need to solve the horizontal and vertical polarization electromagnetic wave, respectively, and perform vector superposition to obtain the final elliptically polarized wave solution. Note that in (25) and (26), $\sum_j \mathbf{L}_{ij}\boldsymbol{\tau}_{TEinc,j}$ and $\sum_j \mathbf{L}_{ij}\boldsymbol{\tau}_{TMinc,j}$ are calculated only once when the system matrices are assembled, and we only need to generate a new set of $\boldsymbol{\Lambda}_{\varphi_1,i}$ and $\boldsymbol{\Lambda}_{\varphi_2,i}$ at each time step. As thus, the spatial connection of the basis functions from different subdomains can be pre-stored, and it is independent of the time function of the incident plane wave. Another advantage of this approach is the multiple functionalities of the shared interface: it plays the roles of the TF/SF interface, Riemann

solver interface, and non-conforming mesh connector. Finally, by controlling the amplitude and phase of two orthogonal linearly polarized waves, one can realize the introduction of plane waves with different polarization characteristics such as linear polarization, circular polarization, and elliptical polarization.

3. NUMERICAL RESULTS AND DISCUSSIONS

3.1. Single-Frequency Circularly Polarized Plane Waves in Free Space

To verify the accuracy of the proposed algorithm, we first investigate the single-frequency circularly polarized plane wave propagation problem. The computational domain is vacuum with a size of $(3\times3\times3)$ m, and the MPML is used for the truncation. The cell size is 0.5 m with 3-order basis functions. Thus, the PPW (points per wavelength) is more than 10 which is enough for this simulation. A plane wave that utilizes a sine/cosine signal as excitation source is incident along the $x+$ direction, with frequency of 155 MHz. The red domain and green domain respectively represent the MPML and the physical region, and the receiver is located in (0.2, 0, 0), as shown in Fig. 2.

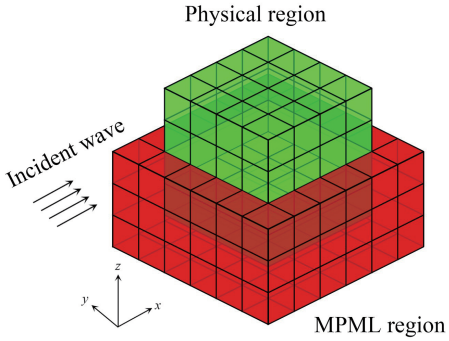

Figure 2. Computational domain of free space with $x+$ direction incident wave. The red and green domain represent the MPML and the physical region, respectively.

To generate left-handed or right-handed circularly polarized plane waves, we can set the phase difference ($\pm90^\circ$) of the two orthogonal incident-field components. In this case, the left-handed circularly polarized wave with wave vector $\mathbf{k}$ along the $x+$ direction was injected in the computational domain by the vector superposition of two orthogonal fields: y-polarized plane wave incidents along the $x+$ direction with cosine signal as the excitation function; z-polarized plane wave incidents along the $x+$ direction with sinusoidal signal as the excitation function. The phase difference $\varphi_y - \varphi_z = \pi/2$. Using the DGTD algorithm proposed in this work, we can obtain the electromagnetic field value at the receiver, as illustrated in Fig. 3. Figs. 3(a)–3(b) represent y- and z-components of the electric field intensity at the receiving point, respectively. It can be seen that the calculated results of the proposed method agree well with the analytical solution. Figs. 3(c)–3(d) show the relative errors of electric field intensity and magnetic flux density calculated by the proposed method, respectively. We can see that the relative error is below -40 dB except for the high frequency pollution part. Note that, when the cosine signal component is first added into the plane wave, the system responds jump from zero state to the maximum value of cosine wave, giving rise to the so-called high-frequency pollution phenomenon. However, as the simulation process tends to be stable, the DGTD solution shows good agreement with the reference.

In addition, along the propagation direction of wave vector, it can be seen that the vector of electric field on the plane perpendicular to the propagation direction has circular polarization characteristics of single-frequency signal, as shown in Fig. 4(a). Receiver I to Receiver VI represent the 3D electric field vectors at six receivers (0, 0, 0) m, (0.1, 0, 0) m, (0.2, 0, 0) m, (0.3, 0, 0) m, (0.4, 0, 0) m, and (0.5, 0, 0) m along the propagation direction, and we can see that circularly polarized waves generated here conform to the left hand helix rule. On top of that, Fig. 4(b) shows the electric field vector in the plane perpendicular to the propagation direction. We can see that the track of the electric field vector is circular, which also verifies the circular polarization characteristics of this single-frequency signal.

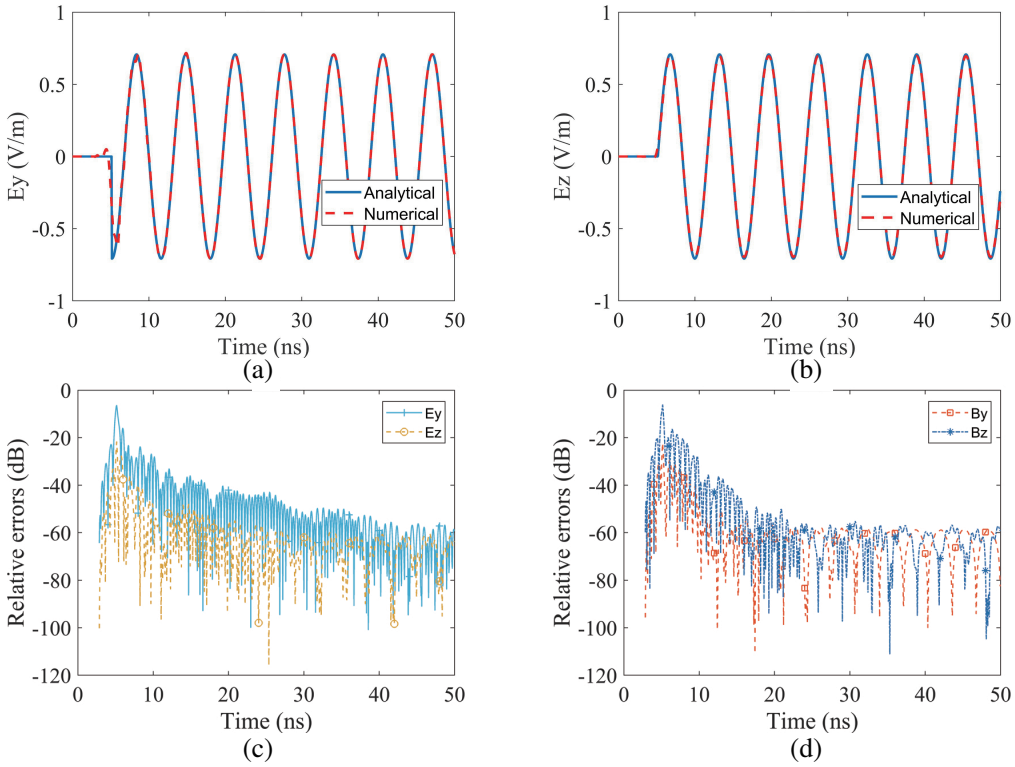

Figure 3. Comparison of left-handed circularly polarized waves obtained by the proposed method and the analytical solution. (a) y-component of he electric field intensity at the receiving point. (b) z-component of the electric field intensity. (c) Relative error of electric field intensity. (d) Relative error of magnetic flux density.

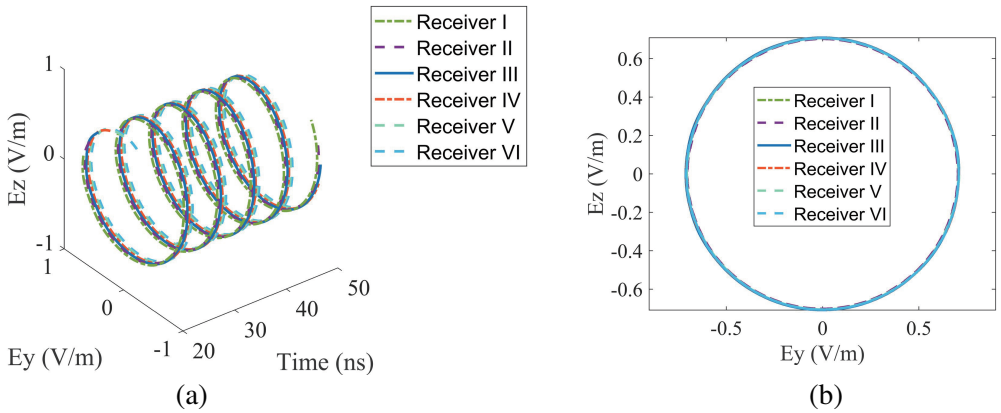

Figure 4. Implementation of left-handed circularly polarized wave. (a) 3D electric field vectors at six receivers. (b) Electric field vectors in the plane perpendicular to the propagation direction.

Similarly, we can generate right-handed circularly polarized plane waves: z-polarized plane wave incidents along the $x+$ direction with cosine signal as the excitation function, combining y-polarized plane wave incidents along the $x+$ direction with sinusoidal signal as the excitation function, with these two waves' phase difference $\varphi_y - \varphi_z = -\pi/2$, and Figs. 5(a)–5(b) represent y- and z-components of the electric field intensity at the receiving point, respectively. We can seen that the DGTD results agree well with the analytical solution. Figs. 5(c)–5(d) show the relative errors of electric field intensity and magnetic flux density calculated by the proposed method, respectively.

Furthermore, Fig. 6(a) exhibits the 3D electric field vectors at six receivers located along the

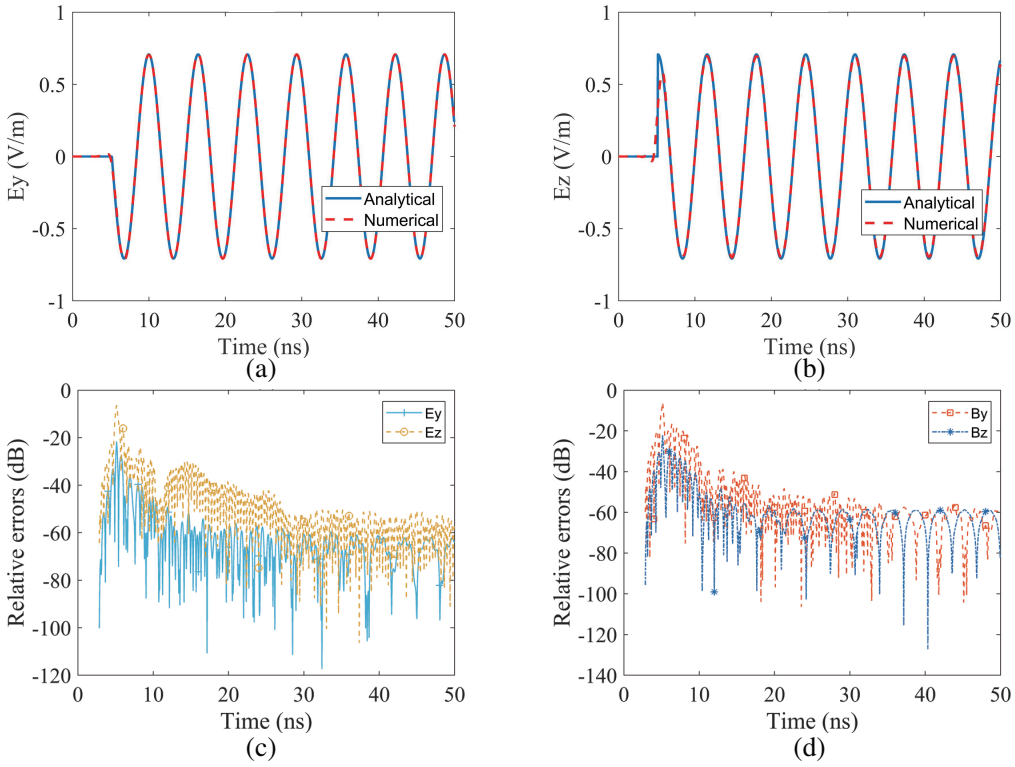

Figure 5. Comparison of right-handed circularly polarized waves obtained by the proposed method and the analytical solution. (a) y-component of the electric field intensity at the receiving point. (b) z-component of the electric field intensity. (c) Relative error of electric field intensity. (d) Relative error of magnetic flux density.

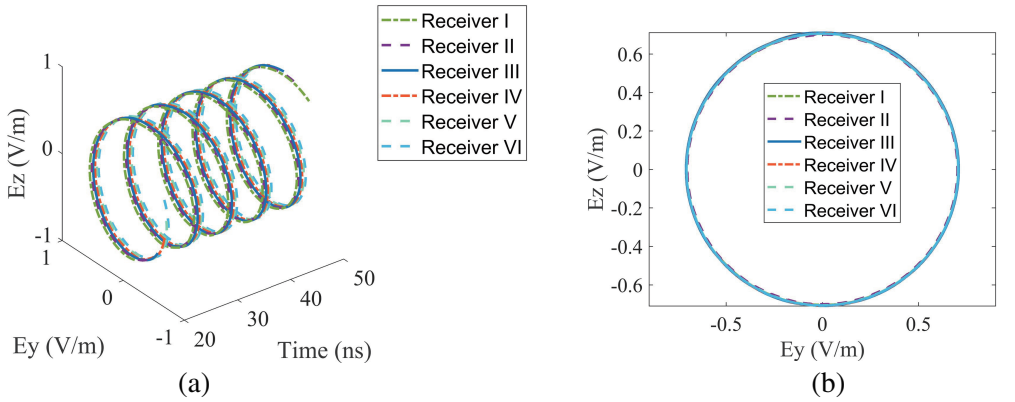

Figure 6. Implementation of right-handed circularly polarized wave. (a) 3D electric field vectors at six receivers. (b) Electric field vectors in the plane perpendicular to the propagation direction.

propagation direction, and it can be seen that circularly polarized waves generated here conform to the right hand helix rule. On top of that, Fig. 6(b) demonstrates the electric field vector in the plane perpendicular to the propagation direction. We can see that the track of the electric field vector is circular, which also verifies the circular polarization characteristics of the incident wave.

3.2. Broadband Circularly Polarized Plane Waves in Free Space

In this section, we further investigate the broadband circularly polarized plane wave propagation problems. The computational domain is the same as previous example, and a plane wave is incident along the $x+$ direction. To inject bandwidth circularly polarized waves, we use a sinusoidal/cosinoidal modulated Gaussian waveform as an excitation signal with centre frequency of 155 MHz. The degree of freedom (DoF) in this model is 251286; the memory consumption is 2704 M; the time consumption is 13.1 minutes; and the average relative error with the analytical solution is about -130 dB.

The left-handed broadband circularly polarized wave with wave vector $\mathbf{k}$ along the $x+$ direction was generated by the vector superposition of two orthogonal fields: y-polarized plane wave with cosinoidal modulated Gaussian waveform as the excitation function and z-polarized plane wave with sinusoidal modulated Gaussian waveform as the excitation function. The phase difference $\varphi_y - \varphi_z = \pi/2$. The electromagnetic fields at the receiver (0.2, 0, 0) m were calculated via the DGTD algorithm, as illustrated in Fig. 7.

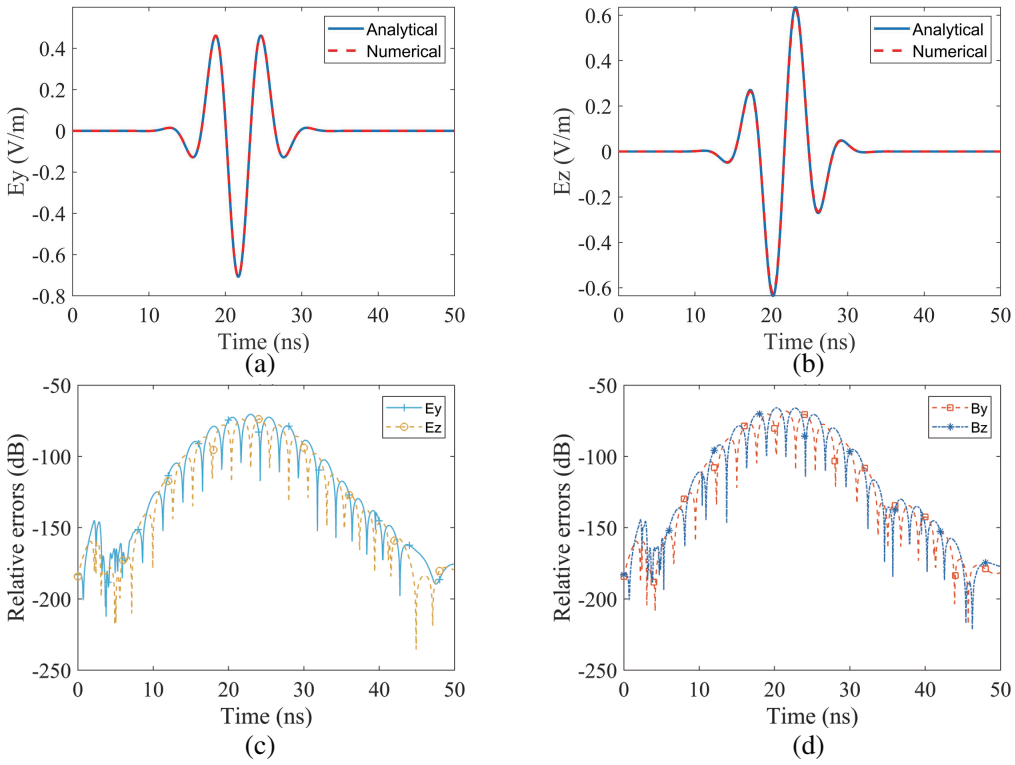

Figure 7. Comparison of left-handed broadband circularly polarized waves obtained by the proposed method and the analytical solution. (a) y-component of the electric field intensity at the receiving point. (b) z-component of the electric field intensity. (c) relative error of electric field intensity. (d) relative error of magnetic flux density.

Figures 7(a)–7(b) represent y- and z-components of the electric field intensity, respectively. It can be seen that the calculated results of the proposed method agree well with the references. Because the modulated Gaussian signal was introduced, there is no high-frequency pollution phenomenon. Figs. 7(c)–7(d) show the relative errors of electric field intensity and magnetic flux density calculated by the proposed method, respectively. We can see that the relative error is below -60 dB indicating the accuracy of this method.

In addition, along the propagation direction of wave vector, it can be seen that the electric-field vectors on the plane perpendicular to the propagation direction have circular polarization characteristics of broadband signals, as shown in Fig. 8(a). Receiver I to Receiver VI represent the 3D electric field

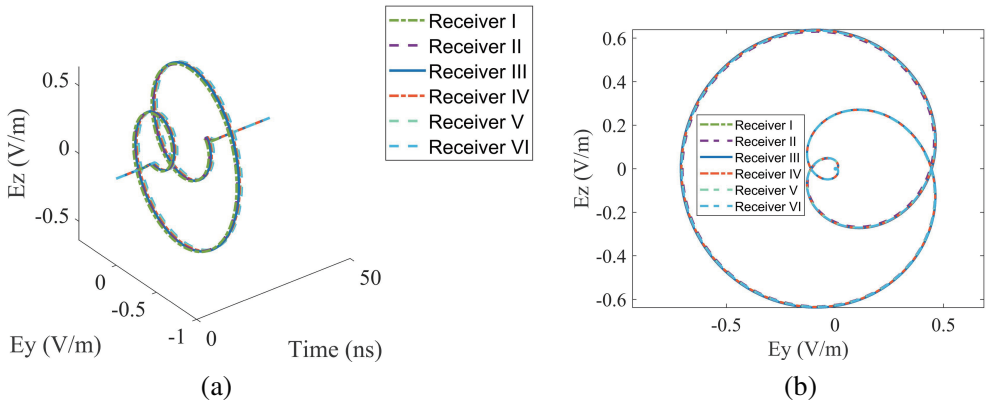

Figure 8. Implementation of left-handed broadband circularly polarized wave. (a) 3D electric field vectors at six receivers. (b) Electric field vectors in the plane perpendicular to the propagation direction.

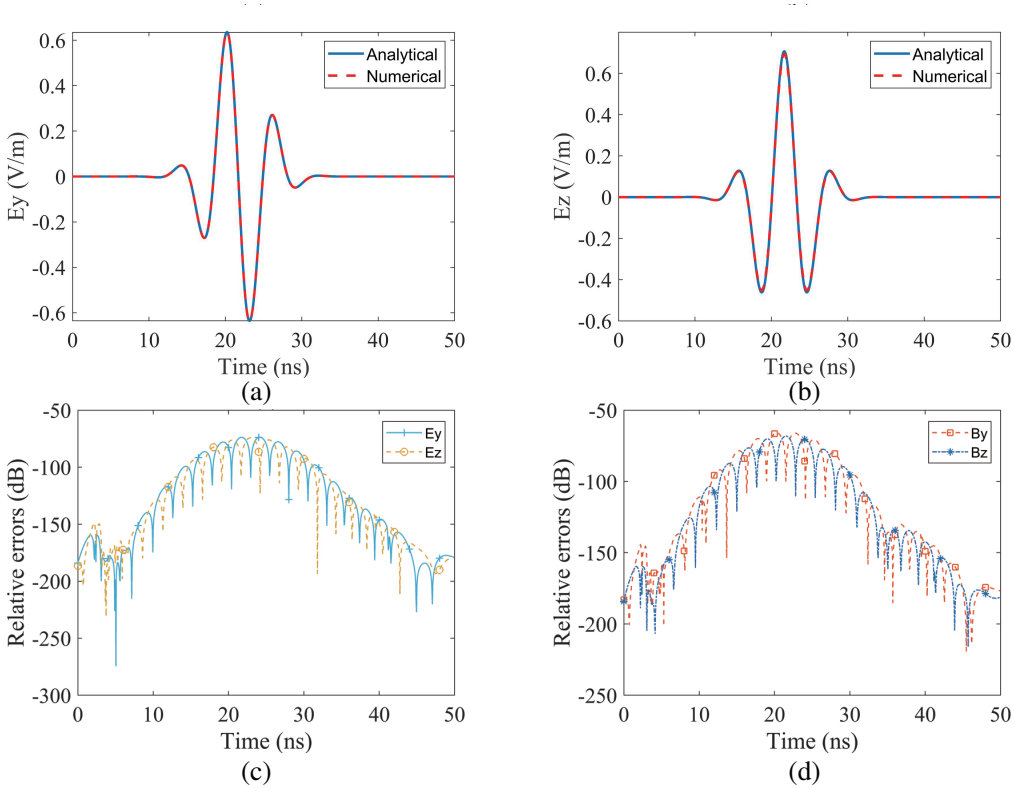

Figure 9. Comparison of right-handed broadband circularly polarized waves obtained by the proposed method and the analytical solution. (a) y-component of the electric field intensity at the receiving point. (b) z-component of the electric field intensity. (c) Relative error of electric field intensity. (d) Relative error of magnetic flux density.

vectors at six receivers (0, 0, 0) m, (0.1, 0, 0) m, (0.2, 0, 0) m, (0.3, 0, 0) m, (0.4, 0, 0) m, and (0.5, 0, 0) m along the propagation direction, and we can see that the broadband circularly polarized waves generated here conform to the left hand helix rule. Besides, Fig. 8(b) shows the electric field vectors in the plane perpendicular to the propagation direction, which verifies the broadband circular polarization characteristics.

Similarly, we can generate right-handed broadband circularly polarized plane waves, and Fig. 9 shows the comparison results and relative errors comparison. Fig. 10(a) exhibits the 3D electric field

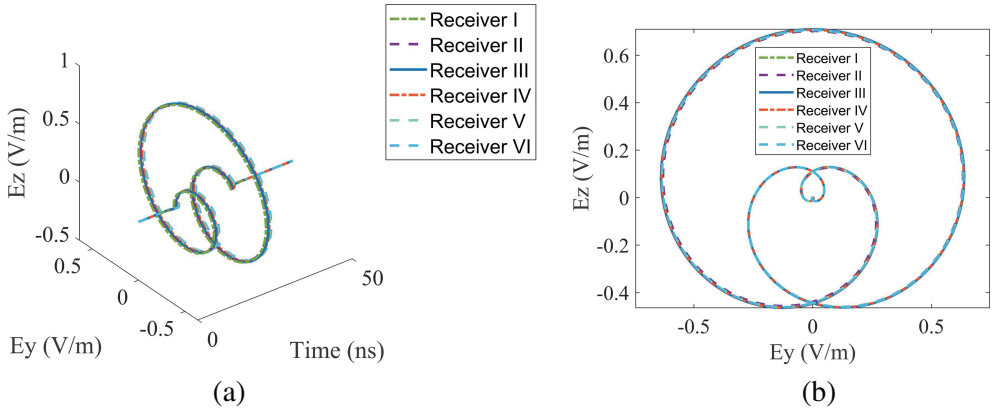

Figure 10. Implementation of right-handed broadband circularly polarized wave. (a) 3D electric field vectors at six receivers. (b) Electric field vectors in the plane perpendicular to the propagation direction.

vectors at six receivers located along the propagation direction, and it can be seen that broadband circularly polarized waves generated here conform to the right hand helix rule. Finally, Fig. 10(b) demonstrates the electric field vectors in the plane perpendicular to the propagation direction, which verifies the broadband circular polarization characteristics of the incident wave.

3.3. Superposition of Two Broadband Circularly Polarized Waves

To demonstrate the vector superposition relationship of two circularly polarized waves, we perform linear superposition of broadband left-handed and right-handed polarized waves at the above six receivers. Fig. 11(a) shows the 3D electric field vectors generated by the superposition, and we can see that the resultant field still has the characteristics of Gaussian signal. Meanwhile, the waveform also shows the characteristics of linear polarization, as we can see in Fig. 11(b), which is a view in the polarization plane. As we know, linearly polarized waves can be decomposed into two circularly polarized waves with opposite rotation with 90° phase difference. Meanwhile, circular polarization can also be synthesized by linear superposition of orthogonal linearly polarized waves with 90° phase difference.

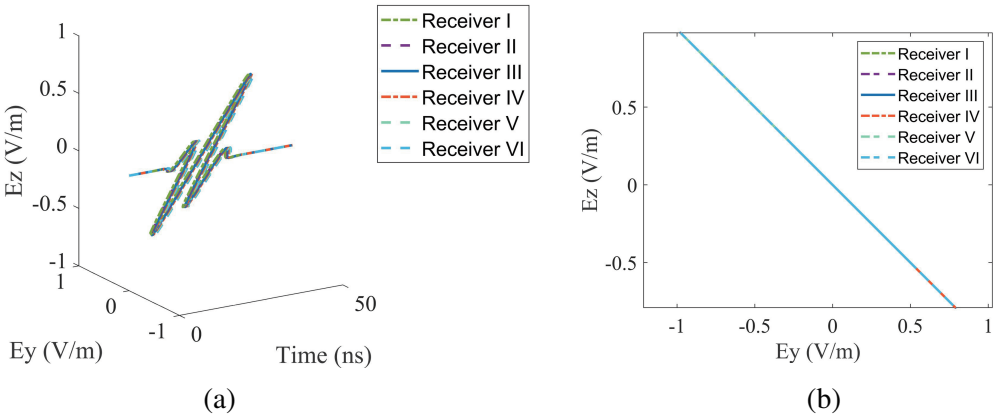

Figure 11. Vector superposition of two opposite rotation circularly polarized waves. (a) 3D electric field vectors at six receivers. (b) Electric field vectors in the polarization plane.

3.4. NASA Almond Illuminated by Elliptically Polarized Waves

Finally, we investigate scattering properties of a NASA Almond with size length (1.262×0.488×0.1626) m embedded in the above computational domain, as illustrated in Fig. 12. Tetrahedral meshes are

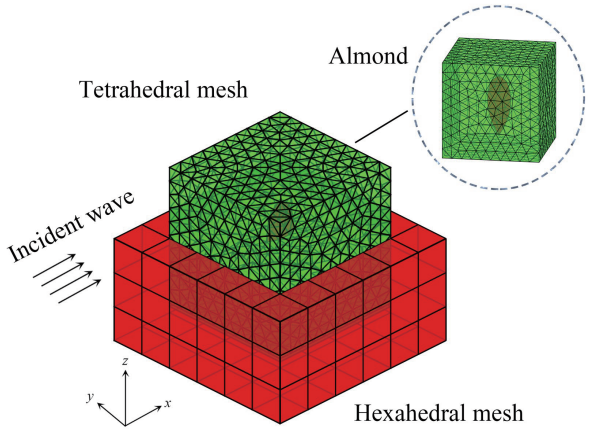

Figure 12. Computational domain for the investigation on scattering characteristics of a NASA Almond with different incident waves. The red and green domain represent the MPML and the physical region, respectively.

employed to construct the Almond and the physical region, while the hexahedral meshes are used to build the MPML region. The tetrahedral cell size is about 0.2 m with 2-order basis functions. Thus, the PPW in vacuum is about 20. Plane waves are injected into the DGTD method via the TF/SF boundary. The broadband elliptically polarized plane waves are incident along the $x+$ direction with centre frequency of 155 MHz, and the receiver is located at $(-0.2,\ 0.2,\ -0.2)$ m.

Utilizing DGTD method, we investigated the scattering field distribution of the Almond illuminated by different incident waves: TE mode with modulated Gaussian waveform, TM mode with modulated Gaussian waveform, and elliptically polarized waves.

Figure 13 shows the electric field components on the receiver illuminated by the broadband left-handed elliptically polarized waves and the corresponding TE and TM incident waves, i.e., this left-handed elliptically polarized waves can be decomposed into these two components (TE component with amplitude 1 V/m and TM component with amplitude 0.7071 V/m). Similarly, Fig. 14 shows the electric field components illuminated by the right-handed elliptically polarized waves and the corresponding TE and TM incident waves. Note that the left-handed TE (or TM) wave is not the same as the right-handed TE (or TM) wave, as the initial phases are different. Numerical experiments demonstrate that the scattering fields of the anomaly illuminated by different polarization waves show great differences as expected. These polarization waves in the scattered wave contains rich characteristic information of the target's appearance structure, which may greatly improve the ability of target recognition and detection.

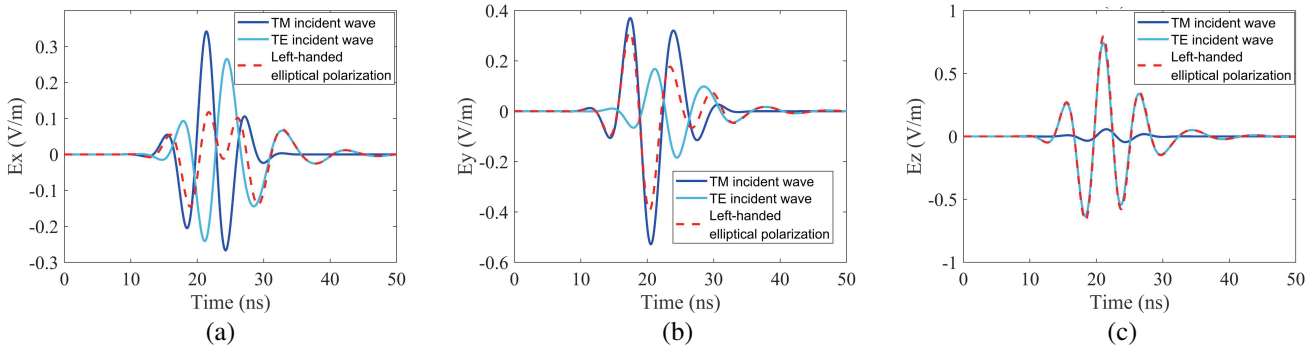

Figure 13. Electric field components illuminated by the TM, TE incident waves and left-handed elliptically polarized waves (a) x-component of the electric field. (b) y-component of the electric field. (b) z-component of the electric field.

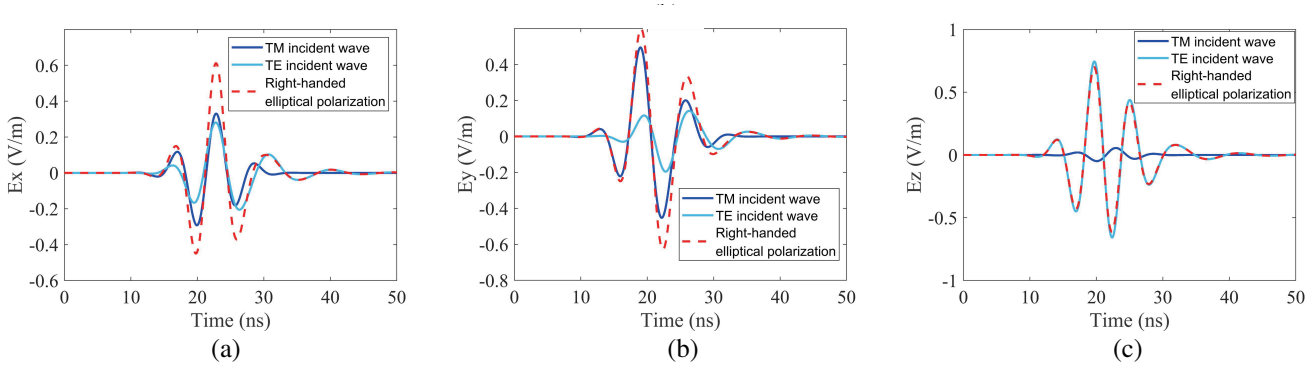

Figure 14. Electric field components illuminated by the TM, TE incident waves and right-handed elliptically polarized waves (a) x-component of the electric field. (b) y-component of the electric field. (b) z-component of the electric field.

4. CONCLUSION

This research investigated an efficient approach of analytical solution for elliptically polarized plane wave injection using Discontinuous Galerkin Time-Domain (DGTD) algorithm through total-field/scattered-field (TF/SF) boundary. The methodology is performed by employing the non-conformal DGTD approach with a Riemann solver at the subdomain level. A detailed analysis is conducted on the suggested approach of elliptically polarized wave injection implemented through the explicit fourth order Runge-Kutta (RK4) time integration scheme, and several evaluating parameters are considered as shown in results to validate the effectiveness. The experimental results and numerical outcomes declare the significance of suggested approach, and it can definitely enhance the capability to estimate the numerical solutions for the characteristics of elliptically polarized waves.

DECLARATIONS

Competing Interests , The authors have no financial or proprietary interests in any material discussed in this article.

Data Availability

The datasets generated during and/or analysed during the current study are available from the corresponding author on reasonable request.

REFERENCES

1. Merewether, E., R. Fisher, and F. W. Smith, "On implementing a numeric Huygen's source scheme in a finite difference program to illuminate scattering bodies," *IEEE Trans. Nucl. Sci.*, Vol. 27, No. 6, 1829–1833, Dec. 1980.
2. Taflove, A. and S. C. Hagness, *Computational Electrodynamics: The Finite-Difference Time-Domain Method*, Artech House, Boston, 2005.
3. Schneider, J. B., "Plane waves in FDTD simulations and a nearly perfect total-field/scattered-field boundary," *IEEE Trans. Antennas Propag.*, Vol. 52, No. 12, 3280–3287, Dec. 2004.
4. Hadi, M. F., "A versatile split-field 1-D propagator for perfect plane wave injection," *IEEE Trans. Antennas Propag.*, Vol. 57, No. 9, 2691–2697, Sept. 2009.
5. Tan, T. and M. Potter, "Optimized analytic filed propagator(O-AFP) for plane wave injection in FDTD simulations," *IEEE Trans. Antennas Propag.*, Vol. 58, No. 3, 824–831, Mar. 2010.

6. Tan, T. and M. Potter, "FDTD discrete plane wave(FDTD-DPW) formulation for a perfectly matched source in TFSF simulations," *IEEE Trans. Antennas Propag.*, Vol. 58, No. 8, 2641–2648, Aug. 2010.
7. Anantha, V. and A. Taflove, "Efficient modeling of infinite scatterers using a generalized total-field/scattered-field FDTD boundary partially embedded within PML," *IEEE Trans. Antennas Propag.*, Vol. 50, No. 10, 1111–1119, Oct. 2002.
8. Capoglu, I. R. and G. S. Smith, "A total-field/scattered-field plane wave source for the FDTD analysis of layered media," *IEEE Trans. Antennas Propag.*, Vol. 56, No. 1, 158–169, Jan. 2008.
9. Riley, D. J., J. M. Jin, Z. Lou, and L. E. R. Petersson, "Total-and scattered-field decomposition technique for the finite-element time-domain method," *IEEE Trans. Antennas Propag.*, Vol. 54, No. 1, 35–41, Jan. 2006.
10. Yang, Q., B. Wei, L. Li, and D. Ge, "Implementation of corner-free truncation strategy in DGTD method," *Waves Random Complex Media.*, Vol. 27, No. 2, 367–380, Apr. 2017.
11. Alvarez, J., L. D. Angulo, A. R. Bretones, and S. G. Garcia, "3-D Discontinuous Galerk in time-domain method for anisotropic materials," *IEEE Antennas Wireless Propag. Lett.*, Vol. 11, 1182–1185, 2012.
12. Bao, H., L. Kang, S. D. Campbell, and D. H. Werner, "PML implementation in a nonconforming mixed-element DGTD method for periodic structureanalysis," *IEEE Trans. Antennas Propag.*, Vol. 67, No. 11, 6979–6988, Nov. 2019.
13. Alvarez, J., L. D. Angulo, M. R. Cabello, A. R. Bretones, and S. G. Garcia, "Ananalysis of the leap-frog discontinuous Galerkin method for Maxwell's equations," *IEEE Trans. Microw. Theory Tech.*, Vol. 62, No. 2, 197–207, Feb. 2014.
14. Ren, Q., Q. Zhan, and Q. H. Liu, "An improved subdomain level nonconformal discontinuous galerkin time domain (DGTD) method for materials with full-tensor constitutive parameters," *IEEE Photon. J.*, Vol. 9, No. 2, 1–13, Apr. 2017.
15. Dosopoulos, S. and J.-F. Lee, "Interior penalty discontinuous galerkin finite element method for the time-dependent first order maxwell's equations," *IEEE Trans. Antennas Propag.*, Vol. 58, No. 12, 4085–4090, Dec. 2010.
16. Li, P., Y. Shi, L. J. Jiang, and H. Bağci, "DGTD analysis of electromagnetic scattering from penetrable conductive objects with IBC," *IEEE Trans. Antennas Propag.*, Vol. 63, No. 12, 5686–5697, Dec. 2015.
17. Li, P., L. J. Jiang, and H. Bağci, "Discontinuous galerkin time-domain modeling of graphene nanoribbon incorporating the spatial dispersion effects," *IEEE Trans. Antennas Propag.*, Vol. 66, No. 7, 3590–3598, July 2018.
18. Yang, Q., B. Wei, L. Li, and D. Ge, "Simulation of electromagnetic waves in a magnetized cold plasma by the SO-DGTD method," *IEEE Trans. Antennas Propag.*, Vol. 66, No. 8, 4151–4157, Aug. 2018.
19. Wang, P., Y. Shi, Z. G. Ban, S. C. Zhu, Q. Yang, and L. Li, "Penalty fac tor threshold and time step bound estimations for discontinuous Galerkin time-domain method based on Helmholtz equation," *IEEE Trans. Antennas Propag.*, Vol. 68, No. 11, 7494–7506, Nov. 2020.
20. Chen, G., L. Zhao,W. Yu, S. Yan, K. Zhang, and J. Jin, "A general scheme for the discontinuous Galerkin time-domain modeling and s-parameter extraction of inhomogeneous waveports," *IEEE Trans. Microw. Theory Techn.*, Vol. 66, No. 4, 1701–1712, Apr. 2018.
21. Zhang, T., H. Bao, D. Ding, and R. Chen, "Interior penalty DGTD method for solving wave equation in dispersive media described with GDM model," *IEEE Trans. Antennas Propag.*, Vol. 69, No. 9, 6105–6110, Sept. 2021.
22. Gedney, S. D., C. Luo, J. A. Roden, R. D. Crawford, B. Guernsey, J. A. Miller, and E. W. Lucas, "A discontinuous galerkin finite element time domain method with PML," *IEEE Antennas and Propagation Society International Symposium*, 1–4, 2008.
23. Li, K., T. Huang, L. Li, S. Lanteri, L. Xu, and B. Li, "A reduced-order discontinuous Galerkin method based on POD for electromagnetic simulation," *IEEE Trans. Antennas Propag.*, Vol. 66, No. 1, 242–254, Jan. 2018.

24. Sun, Q., R. Zhang, Q. Zhan, and Q. H. Lu, "3D implicit-explicit hybrid finite difference/spectral element/finite element time domain method without a Buffer zone," *IEEE Trans. Antennas Propag.*, Vol. 67, No. 8, 5469–5476, Aug. 2019.
25. Zhan, Q., Y. Wang, Y. Fang, Q. Ren, S. Yang, W. Y. Yin, and Q. H. Liu, "An adaptive high-order transient algorithm to solve large-scale anisotropic Maxwell's equations," *IEEE Trans. Antennas Propag.*, Vol. 70, No. 3, 2082–2092, Mar. 2022.
26. Sankaran, K., C. Fumeaux, and R. Vahldieck, "Cell-centered finite-volume-based perfectly matched layer for time-domain Maxwell system," *IEEE Trans. Microw. Theory Tech.*, Vol. 54, No. 3, 1269–1276, Mar. 2006.
27. Lee, J. F., R. Lee, and A. Cangellaris, "Time-domain finite-element methods," *IEEE Trans. Antennas Propag.*, Vol. 45, No. 3, 430–442, Mar. 1997.
28. Jin, J.-M., *The Finite Element Method in Electromagnetics*, 2nd Edition, Wiley, New York, NY, USA, 2002.
29. Ren, Q., L. E. Tobon, Q. Sun, and Q. H. Liu, "A new 3-D nonspurious discontinuous galerkin spectral element time-domain (DG-SETD) method for Maxwell's equations," *IEEE Trans. Antennas Propag.*, Vol. 63, No. 6, 2585–2594, June 2015.
30. Chen, J., L. E. Tobon, M. Chai, J. A. Mix, and Q. H. Liu, "Efficient implicit-explicit time stepping scheme with domain decomposition for multiscale modeling of layered structures," *IEEE Trans. Compon. Pack. Manuf. Technol.*, Vol. 1, No. 9, 1438–1446, Sept. 2011.
31. Sun, Q., Q. Zhan, Q. Ren, and Q. H. Liu, "Wave equation-based implicit subdomain DGTD method for modeling of electrically small problems," *IEEE Trans. Microw. Theory Techn.*, Vol. 65, No. 4, 1111–1119, Apr. 2017.
32. Wen, P., Q. Ren, J. Chen, A. Chen, and Y. Zhang, "Improved memory-efficient subdomain level discontinuous galerkin time domain method for periodic/quasi-periodic structures," *IEEE Trans. Antennas Propag.*, Vol. 68, No. 11, 7471–7479, Nov. 2020.
33. Zhou, Y., L. Shi, N. Liu, C. Zhu, H. Liu, and Q. H. Liu, "Spectral element method and domain decomposition for low-frequency fubsurface EM simulation," *IEEE Geosci. Remote. Sens. Lett.*, Vol. 13, No. 4, 550–554, Apr. 2016.
34. Zhan, Q., Q. Ren, Q. Sun, H. Chen, and Q. H. Liu, "Isotropic riemann solver for a nonconformal discontinuous galerkin pseudospectral time-domain algorithm," *IEEE Trans. Geosci. Remote. Sens.*, Vol. 55, No. 3, 1254–1261, Mar. 2017.
35. Zhou, Y., L. Shi, N. Liu, C. Zhu, H. Liu, and Q. H. Liu, "Spectral element method and domain decomposition for low-frequency subsurface EM simulation," *IEEE Geosci. Remote Sens. Lett.*, Vol. 13, No. 4, 550–554, Apr. 2016.
36. Shi, L., M. Zhuang, Y. Zhou, N. Liu, and Q. H. Liu, "Domain decomposition based on the spectral element method for frequency-domain computational elastodynamics," *Sci. China Earth Sci.*, Vol. 64, 388–403, 2021.
37. Shi, L., Y. Zhou, J. Wang, M. Zhuang, N. Liu, and Q. H. Liu, "Spectral element method for elastic and acoustic waves in frequency domain," *J. Comput. Phys.*, Vol. 327, No. 15, 19–38, Dec. 2016.
38. Zhan, Q., M. Zhuang, Y. Mao, and Q. H. Liu, "Unified Riemann solution for multi-physics coupling: Anisotropic poroelastic/elastic/fluid interfaces," *Journal of Computational Physics*, Vol. 402, No. 108961, 1–25, Feb. 2020.
39. Zeng, C., J. Xia, R. D. Miller, and G. P. Tsoflias, "Application of the multiaxial perfectly matched layer (M-PML) to near-surface seismic modeling with rayleigh waves," *Geophys.*, Vol. 76, No. 3, T43–T52, May 2011.
40. Meza-Fajardo, K. C. and A. S. Papageorgiou, "On the stability of a non-convolutional perfectly matched layer for isotropic elastic media," *Soil Dyn. Earthq. Eng.*, Vol. 30, No. 3, 68–81, 2010.
41. Zhan, Q., Y. Fang, M. Zhuang, M. Yuan, and Q. H. Liu, "Stabilized DG-PSTD method with nonconformal meshes for electromagnetic waves," *IEEE Trans. Antennas Propag.*, Vol. 68, No. 6, 4714–4726, Jun. 2020.